



1 **Dramatic changes in Harbin aerosol during 2018–2020: the roles of open burning policy and**
2 **secondary aerosol formation**

3 Yuan Cheng¹, Qin-qin Yu¹, Jiu-meng Liu^{1,*}, Xu-bing Cao¹, Ying-jie Zhong¹, Zhen-yu Du², Lin-lin
4 Liang³, Guan-nan Geng⁴, Wan-li Ma¹, Hong Qi¹, Qiang Zhang⁵, Ke-bin He⁴

5 ¹ State Key Laboratory of Urban Water Resource and Environment, School of Environment, Harbin
6 Institute of Technology, Harbin, China

7 ² National Research Center for Environmental Analysis and Measurement, Environmental
8 Development Center of the Ministry of Ecology and Environment, Beijing, China

9 ³ State Key Laboratory of Severe Weather & CMA Key Laboratory of Atmospheric Chemistry,
10 Chinese Academy of Meteorological Sciences, Beijing, China

11 ⁴ State Key Joint Laboratory of Environment Simulation and Pollution Control, School of
12 Environment, Tsinghua University, Beijing, China

13 ⁵ Department of Earth System Science, Tsinghua University, Beijing, China

14 * Corresponding author. Jiu-meng Liu (jiumengliu@hit.edu.cn).

15 **Abstract**

16 Despite the growing interest in understanding haze formation in Chinese megacities, air
17 pollution has been largely overlooked for the Harbin-Changchun (HC) metropolitan area located in
18 the severe cold climate region in Northeast China. In this study, we unfolded significant variations
19 of fine particulate matter (PM_{2.5}) in HC's central city (Harbin) during two sequential heating seasons
20 of 2018–2019 and 2019–2020, and explored major drivers for the observed variations. The two
21 campaigns showed comparable organic carbon (OC) levels but quite different OC sources. The
22 biomass burning (BB) to OC contribution decreased substantially for 2019–2020, which was
23 attributed primarily to the transition of local policies on agricultural fires, i.e., from the “legitimate
24 burning” policy released in 2018 to the “strict prohibition” policy in 2019. Meanwhile, the
25 contribution of secondary OC (OC_{sec}) increased significantly, associated with the much more
26 frequent occurrences of high relative humidity (RH) conditions during the 2019–2020 measurement



27 period. Similar to OC_{sec} , the major secondary inorganic ions, i.e., sulfate, nitrate and ammonium
28 (SNA), also exhibited RH-dependent increases. Given the considerable aerosol water contents
29 predicted for the high-RH conditions, heterogeneous reactions were likely at play in secondary
30 aerosol formation even in the frigid atmosphere in Harbin (e.g., with daily average temperatures
31 down to below $-20\text{ }^{\circ}\text{C}$). In brief, compared to 2018–2019, the 2019–2020 measurement period was
32 characterized by a policy-driven decrease of biomass burning OC, a RH-related increase of OC_{sec}
33 and a RH-related increase of SNA, with the former two factors generally offsetting each other. In
34 addition, we found that open burning activities were actually not eliminated by the “strict prohibition”
35 policy released in 2019, based on a synthesis of air quality data and fire count results. Although not
36 evident throughout the 2019–2020 measurement period, agricultural fires broke out within a short
37 period before crop planting in spring of 2020, and resulted in off-the-chart air pollution for Harbin,
38 with 1- and 24-hour $PM_{2.5}$ concentrations peaking at ~ 2350 and $900\text{ }\mu\text{g}/\text{m}^3$, respectively. This study
39 indicates that sustainable use of crop residues remains a difficult challenge for the massive
40 agricultural sector in Northeast China.



41 1. Introduction

42 Despite nationwide reductions in anthropogenic emissions (Zhang et al., 2019), severe haze
43 pollution characterized by high concentrations of fine particulate matter ($PM_{2.5}$) is far from being
44 effectively controlled in China, e.g., haze episodes were observed in Beijing even during the
45 COVID-19 lockdown (Lv et al., 2020). This reveals the complex yet poorly understood responses
46 of air pollution to changes of primary emission. While secondary aerosol production has been
47 thought to be largely responsible for this lack of understanding, the chemical mechanisms remain
48 vague (Le et al., 2020; Wang et al., 2020b; Huang et al., 2021). For example, state-of-the-art models
49 incorporating gas-phase and cloud chemistry frequently underestimated sulfate and secondary
50 organic aerosol (SOA) concentrations for winter haze events in Beijing (Wang et al., 2014; Zheng
51 et al., 2015a; Cheng et al., 2016; Liu et al., 2020a). The underestimation was more significant with
52 increasing relative humidity (RH) or aerosol water content (AWC) levels, pointing to the importance
53 of aqueous-phase reactions in aerosol water (Wang et al., 2016; Shrivastava et al., 2017; Su et al.,
54 2020; Liu et al., 2021). On the other hand, quantitative prediction of secondary aerosol formed
55 through aqueous-phase reactions remains challenging, partially due to uncertainties in aerosol pH
56 (Guo et al., 2017; Song et al., 2018; Zheng et al., 2020) and oxidant concentrations (Ye et al., 2018;
57 Wang et al., 2020a). In addition, despite the role of heterogeneous chemistry has been widely
58 accepted for sulfate formation, the effects on SOA remain unclear, with more evidences indicating
59 an enhancement effect (Hu et al., 2016; Kuang et al., 2020; Liu et al., 2020a; Wang et al., 2021a)
60 overwhelming those suggesting little influence of RH or AWC on SOA formation (Zheng et al.,
61 2015b). In all, there is a growing interest in understanding haze pollution in Chinese megacities (Shi
62 et al., 2019), especially regarding the driving factors responsible for the spatio-temporal variations,



63 since these factors are essential for the development of efficient air pollution control strategies.

64 Studies on haze in China have been historically concentrated in the North China Plain (NCP),
65 especially around Beijing. Recently, new hotspots began to emerge, e.g., the Harbin-Changchun
66 (HC) metropolitan area. HC is located in the severe cold climate region in Northeast China, and
67 includes 11 cities in the two provinces of Heilongjiang and Jilin. Compared to NCP and other
68 traditional hotspots of air pollution research (e.g., the Yangtze River Delta), HC is characterized by
69 its extremely cold winter when the daily average temperatures could drop to below -20°C . Thus,
70 the heating season is usually as long as six months in HC, lasting from late fall through early spring
71 of next year. During this period, intensive energy use is expected, e.g., coal combustion for central
72 heating in urban areas and household biomass burning for space-heating in rural areas. The intensive
73 energy use, to a large extent, determines the relatively high baseline of $\text{PM}_{2.5}$ pollution in HC's
74 heating season. According to the open access air quality data routinely published by China National
75 Environmental Monitoring Center (<http://106.37.208.233:20035/>), the monthly averages of $\text{PM}_{2.5}$
76 measured during winter in Harbin stayed above $55\ \mu\text{g}/\text{m}^3$ from 2013 throughout 2020, whereas the
77 corresponding value could drop to below $30\ \mu\text{g}/\text{m}^3$ for Beijing.

78 Another feature of HC is that it is located in a main agricultural region in China. For example,
79 Heilongjiang Province provided $\sim 13\%$ and 15% of the national rice and corn productions in 2019,
80 respectively, with only $\sim 5\%$ of China's land area (National Bureau of Statistics of China, 2020).
81 The massive agricultural sector results in a huge amount of crop residues, which are produced after
82 harvesting in autumn and must be disposed before planting in spring of the next year. Although
83 nominally prohibited, open burning persists as an important approach for the disposal of crop
84 residues in Northeast China, with a time window largely overlapped with the heating season. These



85 agricultural fires frequently resulted in heavily-polluted $PM_{2.5}$ episodes, e.g., with 24-hour $PM_{2.5}$
86 peaking at $\sim 650 \mu\text{g}/\text{m}^3$ during early November of 2015 in Harbin (Li et al., 2019b). Given that the
87 agricultural fires were never eliminated, interim provisions were released by Heilongjiang Province
88 in 2018, which approved a window of approximately 3 months (from 11 December, 2018 to 9 March,
89 2019) for open burning of crop residues (Department of Ecology and Environment of Heilongjiang
90 Province, 2018). However, the interim provisions were amended in 2019, i.e., the “legitimate
91 burning” policy was terminated and was replaced by a toughest-ever policy on open burning, which
92 required that agricultural fires should be strictly prohibited for the period of 15 September, 2019 to
93 15 May, 2020. The rapid transition of open burning policy reflects the ongoing attempts of local
94 government to control the severe haze pollution caused by agricultural fires. However, the most
95 effective and reliable approach remains inconclusive, given that very little is known about the role
96 of biomass burning in $PM_{2.5}$ pollution in Northeast China. Actually, $PM_{2.5}$ in Northeast China is far
97 from being well characterized yet with the limited studies, especially regarding sources and
98 chemical mechanisms of aerosol formation.

99 In this study, we investigated the variations of Harbin aerosol during two sequential heating
100 seasons of 2018–2019 and 2019–2020, with focuses on the roles of (1) rapid transition of open
101 burning policy and (2) significant change of meteorological conditions (especially relative
102 humidity), which would influence primary emissions and secondary aerosol formation, respectively.
103 Policy implications for improving air quality in the HC region were also discussed.

104 2. Methods

105 Two campaigns were conducted at an urban site located in the campus of Harbin Institute of
106 Technology (HIT) during the heating seasons of 2018–2019 (from 16 October, 2018 to 14 April,



107 2019; $N = 180$) and 2019–2020 (from 16 October, 2019 to 4 February, 2020; $N = 112$), following
108 the same sampling and analytical procedures. As described for the 2018–2019 campaign (Cheng et
109 al., 2021), a low-volume sampler operated at a flow rate of 5 L/min was used to collect airborne
110 $PM_{2.5}$ onto pre-baked quartz-fiber filters, and the chemical components quantified included organic
111 carbon (OC), elemental carbon (EC), organic tracers for biomass burning (levoglucosan and
112 mannosan) and water-soluble inorganic ions (sulfate, nitrate, ammonium, etc.). Based on the
113 measured species, $PM_{2.5}$ mass was reconstructed as the sum of organic matter (determined as $1.6 \times$
114 OC), EC and inorganic ions. The reconstructed $PM_{2.5}$ will be specified as $(PM_{2.5})^*$ in the following
115 discussions. In addition to the observational results from HIT, online data sets were used to obtain
116 hourly meteorological data such as temperature and relative humidity (RH), and air quality data
117 including $PM_{2.5}$, inhalable particles (PM_{10}), sulfur dioxide (SO_2), nitrogen dioxide (NO_2), carbon
118 monoxide (CO) and ozone (O_3). Refer to supplementary material for details on the field
119 measurement and collection of additional data.

120 Using levoglucosan as the reference component, the relative abundances of water-soluble
121 potassium (K^+) were found to increase substantially for five samples collected during the Chinese
122 New Year periods in February of 2019 ($N = 2$; Cheng et al., 2021) and in January of 2020 ($N = 3$;
123 [Figure S1](#)), pointing to significant influence of firework emissions. Given that such emissions may
124 result in primary sulfate and nitrate which are difficult to quantify, the firework events were
125 excluded, and the remaining sulfate and nitrate were considered secondary in the following
126 discussions. Correspondingly, the sulfur oxidation ratio (SOR) was determined as the molar ratio of
127 sulfate to the sum of sulfate and SO_2 , and the nitrogen oxidation ratio (NOR) was determined
128 similarly based on nitrate and NO_2 .



129 **3. Results and discussion**

130 **3.1 Variation of biomass burning (BB) OC**

131 Although comparable OC levels were observed during the 2018–2019 and 2019–2020
132 measurement periods (averaging 20.66 ± 18.17 and $20.64 \pm 16.76 \mu\text{gC}/\text{m}^3$, respectively), the former
133 campaign exhibited substantially higher contributions of levoglucosan to OC (Figure 1a). Here we
134 applied the levoglucosan to OC ratio (LG/OC) as the indicator for BB impact, given that the absolute
135 concentrations of ambient levoglucosan could be influenced by other factors in addition to biomass
136 burning (e.g., wind speed and planetary boundary layer height). LG/OC averaged 1.83 ± 1.18 and
137 $1.17 \pm 0.30\%$ (on a basis of carbon mass) during 2018–2019 and 2019–2020, respectively, indicating
138 that the influence of biomass burning was stronger during the former campaign. This difference was
139 mainly caused by the 2018–2019 samples collected during and after the “legitimate burning” periods
140 (periods of P-2 and P-3, with average LG/OC ratios of 2.09 ± 1.42 and $2.15 \pm 0.94\%$, respectively;
141 Figure 1b), whereas the LG/OC ratios observed before the onset of “legitimate burning” (P-1,
142 averaging $1.20 \pm 0.36\%$) were in general comparable with those during the 2019–2020 campaign.

143 Recalling the different open burning policies released in 2018 and 2019, the observed
144 variations of LG/OC appeared to be associated with agricultural fires. According to the relationship
145 between levoglucosan and OC, Cheng et al. (2021) classified the 2018–2019 samples into three
146 groups (Cases A, B and C) with LG/OC ranges of $< 1.5\%$, $1.5\text{--}3.0\%$ and $> 3.0\%$, respectively.
147 Levoglucosan exhibited strong linear correlations with OC for all the three cases ($r \geq 0.95$), with
148 slopes, i.e., $\Delta\text{LG}/\Delta\text{OC}$ (approximately equivalent to LG/OC given the close-to-zero intercepts), of
149 1.1, 2.3 and 5.0%, respectively. The variation of LG/OC across the three cases was inferred to be
150 driven mainly by agricultural fires that had relatively low combustion efficiencies, based on a



151 synthesis of the following evidences (Cheng et al., 2021): (1) the levoglucosan to K^+ ratios and
152 levoglucosan to mannosan ratios observed throughout the 2018–2019 campaign were in line with
153 the characteristics of BB smoke emitted by the burning of crop residues; (2) no dependence of
154 LG/OC on temperature was observed, indicating that the variations of LG/OC could not be
155 explained by biomass burning for household space-heating in rural areas; (3) elevated LG/OC ratios
156 were typically associated with intensive fire counts, i.e., open burning of crop residues, around
157 Harbin; (4) chemical signatures associated with combustion phase exhibited changes toward
158 smoldering-dominated burning from Cases A through C, e.g., $\Delta EC/\Delta CO$ (derived from linear
159 regression of EC on CO) decreased whereas the levoglucosan to K^+ ratios increased. Following
160 Cheng et al. (2021), LG/OC ratios higher than 1.5% were considered an indicator for apparent
161 impacts of agricultural fires around Harbin. As shown in [Figures 1c–1d](#), approximately 50% of the
162 2018–2019 samples exhibited LG/OC above 1.5%, with various fractions for the three periods, i.e.,
163 15, 64 and 71% for P-1, P-2 and P-3 samples, respectively. Thus, apparent impacts of agricultural
164 fires were frequently encountered in the 2018–2019 campaign, particularly after the onset of
165 “legitimate burning”. It is noteworthy that the agricultural fires did not actually disappear after the
166 ending of “legitimate burning” and instead extended to mid-April of 2019. For the 2019–2020
167 campaign, however, only less than 5% of the samples showed LG/OC larger than 1.5% ([Figure 1c](#)),
168 indicating that agricultural fires were almost completely eliminated during the measurement period.

169 Comparison of source apportionment results between the two campaigns also indicated
170 substantial changes in the influence of agricultural fires. In this study, source apportionment was
171 performed using EPA’s Positive Matrix Factorization (PMF) model (version 5.0), with OC, EC,
172 levoglucosan, chloride, nitrate, sulfate and ammonium from both campaigns as inputs. A total of



173 five factors were resolved, and their profiles were shown in [Figure S2](#). Two factors (BB-1 and BB-
174 2) were strongly associated with primary biomass burning emissions, since almost all the
175 levoglucosan (~90%) were apportioned to these two factors whereas neither of them was a major
176 contributor to secondary ions. Another two factors were inferred to represent secondary aerosols
177 (SA-1 and SA-2), as they had little EC but the majority of nitrate and sulfate. The last factor (non-
178 BB_{pri}) was attributed to primary emissions from non-BB sources, because more than 50% of EC but
179 little levoglucosan was found in this factor. For the 2018–2019 campaign, both the OC mass
180 apportioned to BB-1 (OC_{BB-1}; [Figure S3](#)) and the contribution of BB-1 to OC (f_{BB-1} ; [Figure 2](#))
181 increased substantially after the onset of “legitimate burning”, likely indicating that this factor was
182 representative of agricultural fire emissions. This inference was also supported by the comparison
183 of OC source apportionment results across the three cases (A–C) with increasing LG/OC ratios, i.e.,
184 with stronger impacts of agricultural fires. OC_{BB-1} increased drastically by ~25 folds (from 1.2 to
185 30.9 $\mu\text{gC}/\text{m}^3$) from Cases A through C, with OC attributed to other factors being largely unchanged,
186 and correspondingly, f_{BB-1} increased sharply from 9 to 69% across the three cases ([Figure S4](#)). In
187 addition, it was noticed that negligible EC was apportioned to the BB-1 factor ([Figure S2](#)), which
188 was the characteristic of smoldering-dominated combustion as supported by numerous BB source
189 emission studies (McMeeking et al., 2009; May et al., 2014; Pokhrel et al., 2016; McClure et al.,
190 2020; Wang et al., 2020c). This feature was consistent with the inference that the agricultural fires
191 had relatively low combustion efficiencies (Cheng et al., 2021). During the 2018–2019 campaign,
192 the contribution of agricultural fires to OC was rather small (9%) before the onset of “legitimate
193 burning”, whereas after this time point, the contribution increased to ~40% ([Figure 2](#)). The overall
194 f_{BB-1} was 34% for the entire measurement period of 2018–2019, suggesting agricultural fire



195 emissions as the dominant source of OC. For the 2019–2020 campaign, however, f_{BB-1} was
196 substantially lower (9%; [Figure 2](#)), comparable with that determined for the 2018–2019 samples
197 collected during P-1, i.e., before the onset of “legitimate burning”. Regarding the temporal variation
198 of agricultural fire impacts, therefore, the same patterns were observed based on the comparisons of
199 LG/OC and PMF results across various measurement periods.

200 Unlike OC_{BB-1} , OC masses apportioned to the BB-2 factor (OC_{BB-2}) were comparable for the
201 2018–2019 samples collected before, during and after the “legitimate burning” periods ([Figure S3](#)).
202 OC_{BB-2} was also largely unchanged across the three cases (A–C) with stronger impacts of
203 agricultural fires ([Figure S4](#)). Therefore, it seems that BB-2 was associated with biomass burning
204 activities that did not have significant daily variation, with the most likely candidate being
205 household combustion of crop residues (for cooking and heating). In addition, OC_{BB-2} appeared to
206 be slightly higher for the 2019–2020 campaign compared to 2018–2019 (6.24 vs. 4.51 $\mu\text{gC}/\text{m}^3$;
207 [Figure S3](#)), presumably because more crop residues were consumed through household use during
208 2019–2020 in response to the “strict prohibition” open burning policy.

209 The two biomass burning factors constituted 57% of OC for the 2018–2019 campaign ([Figure](#)
210 [2](#)). Before the onset of “legitimate burning”, the total contribution of biomass burning (f_{BB}) was 46%
211 and was dominated by the BB-2 factor (i.e., household burning of crop residues), whereas after this
212 time point, f_{BB} increased to 59% and was dominated by BB-1 (agricultural fires). For the Case C
213 samples, i.e., under the strongest impacts of agricultural fires, f_{BB} was as high as 79% ([Figure S4](#)).
214 A prominent reduction in OC_{BB-1} , however, occurred for the 2019–2020 measurement period, and
215 f_{BB} dropped to 39% with BB-2 as the dominant driver ([Figures 2 and S3](#)). It is noteworthy that
216 compared to the typical f_{BB} determined during winter in Beijing (~10–20%, derived from field



217 observations using aerosol mass spectrometer; Hu et al., 2016; Sun et al., 2018; Li et al., 2019a; Xu
218 et al., 2019), the BB contributions were much higher in Harbin even when the contribution of
219 agricultural fires was limited (e.g., during the 2018–2019 campaign, and P-1 in 2018–2019),
220 pointing to strong emissions from residential burning of crop residues throughout the heating season
221 in Northeast China.

222 3.2 Variation of secondary OC

223 OC masses apportioned to the SA-1 and SA-2 factors (OC_{sec}) were considered secondary. OC_{sec}
224 were 3.9 and 7.6 $\mu\text{g}/\text{m}^3$ for the 2018–2019 and 2019–2020 campaigns, respectively, constituting
225 19 and 37% of OC (Figures 2 and S3). It was noticed that for biomass burning OC and OC_{sec} , their
226 inter-campaign differences showed comparable absolute values but opposite signs. This explains
227 why the two heating seasons had significantly different OC sources but almost the same OC average
228 concentrations.

229 As shown in Figure 3, OC_{sec} exhibited a positive dependence on RH, with an explosive increase
230 of OC_{sec} after RH exceeded 80%. Only ~6% of the 2018–2019 samples (10 out of 180) experienced
231 such humid conditions, whereas this fraction was as high as ~37% for 2019–2020 (corresponding
232 to 42 out of the 112 samples). Therefore, the inter-annual variation of OC_{sec} was likely associated
233 with the different RH levels between the two campaigns. Although the daily average temperatures
234 could drop to below $-20\text{ }^\circ\text{C}$ during the measurement periods, simulation results based on the
235 ISORROPIA-II thermodynamic model (see Supplement for details) still showed considerable
236 amounts of liquid water in aerosol-phase at high RH, e.g., typically with AWC levels of above 50
237 $\mu\text{g}/\text{m}^3$ when RH exceeded 80% (Figure 3). Therefore, heterogeneous reactions were presumably at
238 play in the RH-dependent increase of OC_{sec} .



239 [Figure 4](#) compares OC source apportionment results across different RH ranges (< 60%, 60–
240 80% and > 80%), which are termed low-, medium- and high-RH conditions, respectively, for the
241 2019–2020 campaign. Both OC_{sec} and its contribution to OC (f_{sec}) increased significantly from the
242 low- through high-RH conditions, by factors of 9.8 and 2.6, respectively. Although the 2019–2020
243 campaign experienced much lower ambient temperatures compared to Beijing’s winter (~ 0 °C), the
244 f_{sec} of Harbin reached 42% for the RH range of > 80%, generally comparable with the typical range
245 of oxygenated organic aerosol (OOA) contribution (~ 35 –60%) determined under humid winter
246 conditions in Beijing (Sun et al., 2013, 2014, 2018; Hu et al., 2016; Xu et al., 2019).

247 The OC to EC ratio (OC/EC) is a commonly used indicator for SOA, giving rise to the EC-
248 tracer method for the estimation of OC_{sec} mass. However, it has long been recognized that SOA
249 formation is not the only factor that can increase OC/EC, and another factor that could be playing
250 an crucial role is the biomass smoke with relatively high emission ratios of OC to EC. Among the
251 three primary factors resolved in this study, OC/EC for the primary emissions of BB-1 (extremely
252 high as negligible EC was apportioned to this factor; [Figure S2](#)) and BB-2 (3.5) were both larger
253 than that of non-BB_{pri} (2.8). Thus the influences of not only SOA but also biomass burning emissions
254 need to be considered when interpreting the observed OC/EC. For the 2018–2019 campaign, the
255 temporal variation of OC/EC was mainly driven by biomass burning emissions (especially the BB-
256 1 factor), as can be seen from the positive dependence of OC/EC on levoglucosan and the
257 comparison of OC/EC across the three cases with increasing LG/OC ([Figure S5](#)). In this case, the
258 EC-tracer method should be used with caution, since the basic assumption, i.e., variation of OC/EC
259 can be attributed primarily to SOA formation, was invalid. Unlike 2018–2019, SOA was the
260 dominant driver for the variation of OC/EC during the 2019–2020 measurement period, as indicated



261 by positive dependence of OC/EC on sulfate and the comparison of OC/EC across the low- through
262 high-RH conditions (Figure S6). During the 2019–2020 campaign, similar patterns of temporal
263 variation were observed for OC_{sec} retrieved using the EC-tracer method and PMF approach, and
264 both results supported the RH-dependent increase of OC_{sec} (Figure S7). However, compared to the
265 PMF-based f_{sec} , the EC-tracer method resulted in a higher contribution of OC_{sec} to OC for the high-
266 RH conditions (60% vs. 42%). This is not surprising, as variation of biomass burning emissions
267 could also contribute to the elevated OC/EC of the high-RH conditions (Figure S6), but this
268 contribution could not be distinguished from that of SOA by the EC-tracer method. Nonetheless,
269 enhanced SOA formation was evident for the high-RH conditions, which mainly occurred within
270 the coldest months (December and January) during the 2019–2020 measurement period.

271 3.3 Variation of secondary inorganic aerosol

272 Both sulfate and SOR exhibited increasing trends as RH became higher (Figure 5), e.g., SOR
273 averaged 0.09 ± 0.04 and 0.20 ± 0.07 for the RH ranges of below and above 80%, respectively. The
274 apparent increase of SOR after RH exceeded 80% pointed to enhanced sulfate formation,
275 presumably through heterogeneous reactions given the high AWC levels (as can be seen from Figure
276 3). In addition, NO₂ appeared to be at play in the heterogeneous conversion of SO₂ to sulfate,
277 because the RH-dependent increase of SOR was more significant for the samples with relatively
278 high NO₂ concentrations (e.g., above 30 $\mu\text{g}/\text{m}^3$; Figure 6). Based on the observational results
279 available, however, it was inconclusive whether NO₂ was the dominant oxidant for the
280 heterogeneous formation of sulfate. Simulation results by ISORROPIA-II suggested moderately
281 acidic aerosols (pH of 4.2 ± 1.1) for the high-RH conditions, and the importance of other oxidants
282 (e.g., H₂O₂) could be comparable with or even overwhelm NO₂ for the oxidation of SO₂ in aerosol



283 water at such pH levels (Guo et al., 2017; Liu et al., 2017; Ye et al., 2018; Wang et al., 2021b).
284 Nonetheless, the relationship between SOR and RH observed in Harbin was in general consistent
285 with the wintertime results from Beijing. However, the threshold RH for sharp increase of SOR was
286 higher in Harbin (80%) than that in Beijing (~40–70%), and the SOR in Harbin with RH above 80%
287 (averaging 0.2) were at the lower end of those observed during winter in Beijing (typically with
288 averages of ~0.2–0.6) (Sun et al., 2013; Zheng et al., 2015b; Zhang et al., 2018; Li et al., 2019a; Liu
289 et al., 2020b). These differences indicated that heterogeneous formation of sulfate was less efficient
290 in this study, and a likely cause was the relatively low temperatures during the measurement period,
291 which would reduce the rate coefficients of relevant aqueous-phase reactions.

292 The 2018–2019 and 2019–2020 campaigns exhibited comparable sulfate concentrations for the
293 RH range of below 80%, with median values of 3.72 and 3.39 $\mu\text{g}/\text{m}^3$, respectively (Figure S8). RH-
294 dependent increase of sulfate was evident for both campaigns but was less significant for the former
295 one, e.g., the median sulfate were 5.32 and 15.84 $\mu\text{g}/\text{m}^3$ for the high-RH conditions of 2018–2019
296 and 2019–2020, respectively. As mentioned earlier, only 10 out of the 180 samples from the 2018–
297 2019 campaign fell into the high-RH conditions. Among these 10 samples, the RH-dependent
298 increase of sulfate was observed for only three ones with NO_2 concentrations of above 60 $\mu\text{g}/\text{m}^3$,
299 but was not evident for the remaining samples which had much lower NO_2 (mostly below 30 $\mu\text{g}/\text{m}^3$;
300 Figure 7). For the 2019–2020 campaign, however, the majority of the samples with RH above 80%
301 showed NO_2 concentrations of above 60 $\mu\text{g}/\text{m}^3$, accompanied with elevated sulfate. Therefore, the
302 different NO_2 levels under high-RH conditions between the two campaigns (with median
303 concentrations of 21.27 and 72.41 $\mu\text{g}/\text{m}^3$ during 2018–2019 and 2019–2020, respectively; Figure
304 S9) was a likely cause of the more significant RH-dependent increase of sulfate observed during the



305 2019–2020 campaign.

306 The 2019–2020 campaign also exhibited more significant RH-dependent increase of nitrate,
307 similar to sulfate (Figure S10). An obvious difference between the two campaigns was that the
308 nitrate to sulfate ($\text{NO}_3^-/\text{SO}_4^{2-}$) ratios tended to be higher during 2019–2020 (Figure S11), with an
309 average of 1.28 ± 0.51 (compared to 1.10 ± 0.66 for 2018–2019). This trend was somewhat
310 surprising, as the 2019–2020 measurement period experienced substantially lower temperatures
311 than 2018–2019 (Figure S11) and consequently was expected to be impacted by stronger heating-
312 induced coal combustion emissions, which were a large source of SO_2 . However, SO_2 were actually
313 lower for the 2019–2020 campaign, presumably due to the implementation of clean air actions
314 targeting pollutants from coal combustion. On the other hand, NO_2 were higher during 2019–2020.
315 Factors responsible for this increase were unclear, while a possible explanation was that the
316 meteorological conditions of 2019–2020 were generally less favorable for dispersion of air
317 pollutions, as indicated by the frequent occurrences of high RH. In this case, the decrease of SO_2
318 emission in 2019–2020 was inferred to be more significant after accounting for the unfavorable
319 meteorological conditions. In general, the 2019–2020 campaign exhibited higher NO_2 to SO_2 ratios
320 (Figure S11), which were in line with the observed variation of nitrate to sulfate ratios.

321 In addition to the relative abundances of NO_2 and SO_2 , the influence of their gas-to-particle
322 conversion ratios should also be considered when comparing $\text{NO}_3^-/\text{SO}_4^{2-}$ across different conditions.
323 The two campaigns differed with respect to humidity levels and biomass burning emissions, both
324 of which could influence SNA formation. Although NOR and SOR were indeed influenced by RH,
325 $\text{NO}_3^-/\text{SO}_4^{2-}$ did not show clear dependence on RH (Figure S12). In addition, there were
326 observational evidences indicating that biomass burning emissions could enhance photochemical



327 oxidation of NO_2 whereas this effect was much weaker for SO_2 (Akagi et al., 2012; Collier et al.,
328 2016), i.e., stronger BB impacts favor the increase of $\text{NO}_3^-/\text{SO}_4^{2-}$. Therefore, the larger $\text{NO}_3^-/\text{SO}_4^{2-}$
329 during the 2019–2020 campaign could not be explained by the reduced BB influences or the
330 elevated RH levels, and instead should be attributed primarily to the higher NO_2 to SO_2 ratios. The
331 increasing trend of NO_2/SO_2 observed in this study was consistent with inventory results which
332 typically indicated a more rapid decrease of SO_2 emissions compared to NO_2 (Zheng et al., 2018).

333 **3.4 Variation of aerosol composition**

334 The discussions above indicated significant differences between the two campaigns regarding
335 the characteristics of both primary emissions and secondary aerosol formation. This in turn resulted
336 in substantially different aerosol compositions between the two measurement periods, with the
337 dominant drivers for the variation of aerosol composition being different as well (Figure 8).

338 For the 2018–2019 campaign, the contribution of OA to $(\text{PM}_{2.5})^*$ was much higher than that of
339 SNA (60 vs. 28%). The variation of $(\text{PM}_{2.5})^*$ composition was driven mainly by biomass burning
340 emissions (especially those from agricultural fires), which tended to increase the OA contribution
341 and correspondingly decrease the relative abundance of SNA. During the most intensive BB
342 episodes (with LG/OC above 3.0%), the OA contribution reached 66% whereas the SNA
343 contribution dropped to 23%. For the 2019–2020 campaign, however, the contribution of SNA to
344 $(\text{PM}_{2.5})^*$ was largely comparable with OA (41 vs. 49%), and heterogeneous chemistry became the
345 dominant driver for the variation of $(\text{PM}_{2.5})^*$ composition. The relative abundances of both SNA and
346 SOA increased considerably from the low-RH through high-RH conditions, with their total
347 contributions reaching 62% for the RH range of above 80%.

348 During the 2019–2020 measurement period, significantly higher levels of major secondary ions



349 were observed than 2018–2019, i.e., the total concentrations of sulfate, nitrate and ammonium (SNA)
350 averaged 27.30 and 15.53 $\mu\text{g}/\text{m}^3$, respectively. This difference was largely explained by the RH-
351 dependence. For the 2019–2020 campaign, the sampling events with RH above 80% were mainly
352 encountered in January of 2020 ($N = 20$) as well as in December of 2019 ($N = 17$), when the daily
353 average temperatures were typically below -10°C . The frequent occurrences of high RH were
354 uncommon for Harbin's winter, as can be seen from the comparison of RH in January across the
355 past twenty years (Figure 9). Thus, the 2019–2020 campaign provided a unique opportunity to
356 explore heterogeneous chemistry in Chinese cities located in the severe cold climate region, and
357 might be considered as an upper limit regarding the RH-dependent enhancement of secondary
358 aerosols. On the other hand, the effective increase of SNA and SOA under high-RH conditions
359 implied the abundances of gaseous precursors, both organic and inorganic. To avoid the occurrence
360 of extreme pollution events, a more fundamental solution would point to the effective control of
361 gaseous pollutants.

362 **3.5 Agricultural fires missed by the 2019–2020 campaign**

363 The 2019–2020 campaign was designed to cover the entire heating season but was interrupted
364 by the outbreak of COVID-19. Although there was no observational result on aerosol composition
365 after 5 February, 2020, a severe $\text{PM}_{2.5}$ episode caused by agricultural fires was identified during 17–
366 18 April, 2020, as indicated by the intensive fire counts recorded for Harbin and the surrounding
367 areas (Figure 10). According to the open-access air quality data, the 24-hour $\text{PM}_{2.5}$ in Harbin reached
368 ~ 500 and $900 \mu\text{g}/\text{m}^3$ on these two days, respectively, with the hourly concentrations peaking at
369 $\sim 2350 \mu\text{g}/\text{m}^3$. During this period, similarly high $\text{PM}_{2.5}$ levels were observed for a nearby city, Suihua,
370 which is located in the same region (the Song-Nen Plain) as Harbin. Based on a synthesis of air



371 quality data and air mass trajectory, we found that the massive amounts of air pollutants in the
372 Harbin-Suihua region, which were emitted by the agricultural fires within a concentrated period of
373 two days, could be transported ~500 km northward to Heihe, a city located on the border between
374 China and Russia. As shown in [Figures 10 and S13](#), $PM_{2.5}$ in Heihe started to increase when the
375 back trajectory suggested air masses passing over the Harbin-Suihua region, resulting in an episode
376 with a peak $PM_{2.5}$ concentration of $\sim 310 \mu\text{g}/\text{m}^3$. The discussions above indicated that although
377 agricultural fires were not evident during the 2019–2020 measurement period, they were postponed
378 to late April of 2020. Thus, agricultural fires were not actually eliminated by the toughest-ever
379 policy on open burning, but broke out within a short period before the planting of crops in spring
380 instead. It is noteworthy that the intensive open burning activities resulted in not only off-the-chart
381 air pollutions for the nearby cities but also heavily-polluted episodes for downwind regions far away
382 from the source areas. We suggest that transboundary transport of agricultural fire emissions from
383 the Northeast Plain, especially the two provinces of Heilongjiang and Jilin, deserves more attention.

384 **4. Conclusions and implications**

385 Significant differences were observed between aerosol properties measured during two
386 sequential heating seasons in the central city of the HC metropolitan area, i.e., Harbin. Briefly, the
387 differences were caused by inter-annual variations of both primary emissions and secondary aerosol
388 formation. The 2018–2019 measurement period was characterized by (i) frequent occurrences of
389 agricultural fires, which were boosted by the “legitimate burning” policy, and (ii) overall low RH
390 levels which were unfavorable for heterogeneous formation of secondary aerosols. Correspondingly,
391 the observed $(PM_{2.5})^*$ was dominated by organic aerosol, with a substantially higher contribution
392 than SNA (60 vs. 28%). Biomass burning emissions were the largest OC source for this



393 measurement period. The BB to OC contribution (f_{BB}) was 46% before the onset of “legitimate
394 burning” primarily due to household burning of crop residues, and increased to 59% after the onset
395 of “legitimate burning” with the major contribution from agricultural fire emissions. In addition to
396 OC, the temporal variations of $(\text{PM}_{2.5})^*$ mass concentration and chemical composition were mainly
397 driven by biomass burning as well, especially by agricultural fires. The average $(\text{PM}_{2.5})^*$ reached
398 $\sim 100 \mu\text{g}/\text{m}^3$ for the most intensive BB episodes, with an enhanced OA contribution of 66% and a
399 reduced SNA contribution of 23%.

400 Compared to 2018–2019, the 2019–2020 campaign was influenced by (i) a transition of open
401 burning policy, i.e., agricultural fires were strictly prohibited, and (ii) frequent occurrences of high-
402 RH conditions. In this case, no evidence was observed to indicate apparent influence of agricultural
403 fires, and correspondingly, the f_{BB} (39%) was dominated by household burning of crop residues. In
404 addition, both SNA and secondary OC (OC_{sec}) exhibited significant RH-dependent increases. For
405 the RH range of above 80%, SOR and the OC_{sec} to OC contribution reached 0.2 and 42%,
406 respectively, despite the low ambient temperatures encountered (averaging about -16°C in terms of
407 daily average). Unlike 2018–2019, organic aerosol and SNA showed comparable contributions to
408 $(\text{PM}_{2.5})^*$ for the 2019–2020 campaign (49 vs. 41%), and the variations of $(\text{PM}_{2.5})^*$ during this
409 measurement period were mainly driven by secondary components.

410 This study has crucial implications for further improving the air quality in HC region. First, f_{BB}
411 remained relatively high for the heating season of Harbin (e.g., compared to the wintertime results
412 from Beijing), even without apparent influence of agricultural fires. This highlights the importance
413 of reducing domestic use of crop residues, on top of previous clean air actions implemented for the
414 residential sector primarily focusing on coal combustion. Second, driven by the transition of open



415 burning policy, agricultural fires exhibited different patterns but were never eliminated. For example,
416 although there was no “legitimate burning” period during 2019–2020 and agricultural fires did not
417 occur as frequently as during 2018–2019, burning did break out in spring of 2020 before crop
418 planting. Thus, neither the “legitimate burning” policy released in 2018 nor the toughest-ever “strict
419 prohibition” policy released in 2019 could be considered successful for the effective control of
420 agricultural fires. More studies are necessary to design a new roadmap towards sustainable use of
421 crop residues in Northeast China, which may contribute to the dual targets of air quality
422 improvement and climate change mitigation. Third, it is noteworthy that $(PM_{2.5})^*$ averaged ~ 115
423 $\mu\text{g}/\text{m}^3$ for the high-RH conditions of 2019–2020, even higher than results from the most intensive
424 BB episodes during 2018–2019. This reveals the need for effective control of gaseous precursors,
425 both organic and inorganic, of secondary aerosols. Given the increasing trends of NO_2/SO_2 and
426 $\text{NO}_3^-/\text{SO}_4^{2-}$ observed between 2018 and 2020, control of the NO_2 -related sources should be
427 strengthened.

428 **Data availability.**

429 Data are available from the corresponding author upon request (jiumengliu@hit.edu.cn).

430 **Author contribution**

431 YC and JL designed the study and prepared the paper with inputs from all the coauthors. QY, XC,
432 YZ, ZD and LL carried out the experiments. GG provided the air quality data. WM and HQ
433 participated in the field campaign and data analysis. QZ and KB supervised the study.

434 **Competing interests.**

435 The authors declare that they have no conflict of interest.

436 **Acknowledgements**



437 This work was supported by the National Natural Science Foundation of China (41805097), the
438 Natural Science Foundation of Heilongjiang Province (YQ2019D004), the State Key Laboratory of
439 Urban Water Resource and Environment (2020DX14), the State Key Joint Laboratory of
440 Environment Simulation and Pollution Control (19K02ESPCT), the State Environmental Protection
441 Key Laboratory of Sources and Control of Air Pollution Complex (SCAPC202002) and
442 Heilongjiang Touyan Team.

443 **References**

- 444 Akagi, S. K., Craven, J. S., Taylor, J. W., McMeeking, G. R., Yokelson, R. J., Burling, I. R., Urbanski,
445 S. P., Wold, C. E., Seinfeld, J. H., Coe, H., Alvarado, M. J., and Weise, D. R.: Evolution of
446 trace gases and particles emitted by a chaparral fire in California, *Atmos. Chem. Phys.*, 12,
447 1397–1421, 2012.
- 448 Cheng, Y., Yu, Q. Q., Liu, J. M., Du, Z. Y., Liang, L. L., Geng, G. N., Zheng, B., Ma, W. L., Qi, H.,
449 Zhang, Q., and He, K. B.: Strong biomass burning contribution to ambient aerosol during
450 heating season in a megacity in Northeast China: effectiveness of agricultural fire bans?, *Sci.*
451 *Total Environ.*, 754, 142144, 2021.
- 452 Cheng, Y. F., Zheng, G. J., Wei, C., Mu, Q., Zheng, B., Wang, Z. B., Gao, M., Zhang, Q., He, K. B.,
453 Carmichael, G., Pöschl, U., and Su, H.: Reactive nitrogen chemistry in aerosol water as a
454 source of sulfate during haze events in China, *Sci. Adv.*, 2, e1601530, 2016.
- 455 Collier, S., Zhou, S., Onasch, T. B., Jaffe, D. A., Kleinman, L., Sedlacek, A. J., Briggs, N. L., Hee,
456 J., Fortner, E., Shilling, J. E., Worsnop, D., Yokelson, R. J., Parworth, C., Ge, X. L., Xu, J. Z.,
457 Butterfield, Z., Chand, D., Dubey, M. K., Pekour, M. S., Springston, S., and Zhang, Q.:
458 Regional influence of aerosol emissions from wildfires driven by combustion efficiency:
459 insights from the BBOP campaign, *Environ. Sci. Technol.*, 50, 8613–8622, 2016.
- 460 Department of Ecology and Environment of Heilongjiang Province: Interim Provisions of
461 Heilongjiang Province on Reward and Punishment for Straw Open Burning Management,
462 available at: http://www.gov.cn/xinwen/2018-09/15/content_5322298.htm (last access: June
463 17, 2021), 2018.



- 464 Guo, H. Y., Weber, R. J., and Nenes, A.: High levels of ammonia do not raise fine particle pH
465 sufficiently to yield nitrogen oxide-dominated sulfate production, *Sci. Rep.*, 7, 12109, 2017.
- 466 Hu, W. W., Hu, M., Hu, W., Jimenez, J. L., Yuan, B., Chen, W. T., Wang, M., Wu, Y. S., Chen, C.,
467 Wang, Z. B., Peng, J. F., Zeng, L. M., and Shao, M.: Chemical composition, sources, and aging
468 process of submicron aerosols in Beijing: contrast between summer and winter, *J. Geophys.*
469 *Res. Atmos.*, 121, 1955–1977, 2016.
- 470 Huang, X., Ding, A. J., Gao, J., Zheng, B., Zhou, D. R., Qi, X. M., Tang, R., Wang, J. P., Ren, C.
471 H., Nie, W., Chi, X. G., Xu, Z., Chen, L. D., Li, Y. Y., Che, F., Pang, N., Wang, H. K., Tong,
472 D., Qin, W., Cheng, W., Liu, W. J., Fu, Q. Y., Liu, B. X., Chai, F. H., Davis, S. J., Zhang, Q.,
473 and He, K. B.: Enhanced secondary pollution offset reduction of primary emissions during
474 COVID-19 lockdown in China, *Natl. Sci. Rev.*, 8, nwaal37, 2021.
- 475 Kuang, Y., He, Y., Xu, W. Y., Yuan, B., Zhang, G., Ma, Z. Q., Wu, C. H., Wang, C. M., Wang, S. H.,
476 Zhang, S. Y., Tao, J. C., Ma, N., Su, H., Cheng, Y. F., Shao, M., and Sun, Y. L.: Photochemical
477 aqueous-phase reactions induce rapid daytime formation of oxygenated organic aerosol on the
478 North China Plain, *Environ. Sci. Technol.*, 54, 3849–3860, 2020.
- 479 Le, T. H., Wang, Y., Liu, L., Yang, J. N., Yung, Y. L., Li, G. H., and Seinfeld, J. H.: Unexpected air
480 pollution with marked emission reductions during the COVID-19 outbreak in China, *Science*,
481 369, 702–706, 2020.
- 482 Li, H. Y., Cheng, J., Zhang, Q., Zheng, B., Zhang, Y. X., Zheng, G. J., and He, K. B.: Rapid transition
483 in winter aerosol composition in Beijing from 2014 to 2017: response to clean air actions,
484 *Atmos. Chem. Phys.*, 19, 11485–11499, 2019a.
- 485 Li, Y. C., Liu, J., Han, H., Zhao, T. L., Zhang, X., Zhuang, B. L., Wang, T. J., Chen, H. M., Wu, Y.,
486 and Li, M. M.: Collective impacts of biomass burning and synoptic weather on surface PM_{2.5}
487 and CO in Northeast China, *Atmos. Environ.*, 213, 64–80, 2019b.
- 488 Liu, J. M., Wang, P. F., Zhang, H. L., Du, Z. Y., Zheng, B., Yu, Q. Q., Zheng, G. J., Ma, Y. L., Zheng,
489 M., Cheng, Y., Zhang, Q., and He, K. B.: Integration of field observation and air quality
490 modeling to characterize Beijing aerosol in different seasons, *Chemosphere*, 242, 125195,
491 2020a.
- 492 Liu, P. F., Ye, C., Xue, C. Y., Zhang, C. L., Mu, Y. J., and Sun, X.: Formation mechanisms of
493 atmospheric nitrate and sulfate during the winter haze pollution periods in Beijing: gas-phase,



- 494 heterogeneous and aqueous-phase chemistry, *Atmos. Chem. Phys.*, 20, 4153–4165, 2020b.
- 495 Liu, T. Y., Chan, A. W. H., and Abbatt, J. P. D.: Multiphase oxidation of sulfur dioxide in aerosol
496 particles: implications for sulfate formation in polluted environments, *Environ. Sci. Technol.*,
497 8, 4227–4242, 2021.
- 498 Lv, Z. F., Wang, X. T., Deng, F. Y., Ying, Q., Archibald, A. T., Jones, R. L., Ding, Y., Cheng, Y., Fu,
499 M. L., Liu, Y., Man, H. Y., Xue, Z. G., He, K. B., Hao, J. M., and Liu, H.: Source-receptor
500 relationship revealed by the halted traffic and aggravated haze in Beijing during the COVID-
501 19 lockdown, *Environ. Sci. Technol.*, 54, 15660–15670, 2020.
- 502 May, A. A., McMeeking, G. R., Lee, T., Taylor, J. W., Craven, J. S., Burling, I., Sullivan, A. P.,
503 Akagi, S., Collett, J. L., Flynn, M., Coe, H., Urbanski, S. P., Seinfeld, J. H., Yokelson, R. J.,
504 and Kreidenweis, S. M.: Aerosol emissions from prescribed fires in the United States: a
505 synthesis of laboratory and aircraft measurements, *J. Geophys. Res. Atmos.*, 119, 11826–11849,
506 2014.
- 507 McClure, C. D., Lim, C. Y., Hagan, D. H., Kroll, J. H., Cappa, C. D.: Biomass-burning-derived
508 particles from a wide variety of fuels – Part 1: properties of primary particles, *Atmos. Chem.*
509 *Phys.*, 20, 1531–1547, 2020.
- 510 McMeeking, G. R., Kreidenweis, S. M., Baker, S., Carrico, C. M., Chow, J. C., Collett, J. L., Hao,
511 W. M., Holden, A. S., Kirchstetter, T. W., Malm, W. C., Moosmüller, H., Sullivan, A. P., and
512 Wold, C. E.: Emissions of trace gases and aerosols during the open combustion of biomass in
513 the laboratory, *J. Geophys. Res.*, 114, D19210, 2009.
- 514 National Bureau of Statistics of China: China Statistical Yearbook 2020, available at:
515 <http://www.stats.gov.cn/tjsj/ndsj/2020/indexeh.htm>, 2020.
- 516 Pokhrel, R. P., Wagner, N. L., Langridge, J. M., Lack, D. A., Jayarathne, T., Stone, E. A., Stockwell,
517 C. E., Yokelson, R. J., and Murphy, S. M.: Parameterization of single-scattering albedo (SSA)
518 and absorption Ångström exponent (AAE) with EC/OC for aerosol emissions from biomass
519 burning, *Atmos. Chem. Phys.*, 16, 9549–9561, 2016.
- 520 Shi, Z. B., Vu, T., Kotthaus, S., Harrison, R. M., Grimmond, S., Yue, S. Y., Zhu, T., Lee, J., Han, Y.
521 Q., Demuzere, M., Dunmore, R. E., Ren, L. J., Liu, D., Wang, Y. L., Wild, O., Allan, J., Acton,
522 W. J., Barlow, J., Barratt, B., Beddows, D., Bloss, W. J., Calzolari, G., Carruthers, D., Carslaw,
523 D. C., Chan, Q., Chatzidiakou, L., Chen, Y., Crilley, L., Coe, H., Dai, T., Doherty, R., Duan, F.



- 524 K., Fu, P. Q., Ge, B. Z., Ge, M. F., Guan, D. B., Hamilton, J. F., He, K. B., Heal, M., Heard, D.,
525 Hewitt, C. N., Hollaway, M., Hu, M., Ji, D. S., Jiang, X. J., Jones, R., Kalberer, M., Kelly, F.
526 J., Kramer, L., Langford, B., Lin, C., Lewis, A. C., Li, J., Li, W. J., Liu, H., Liu, J. F., Loh, M.,
527 Lu, K. D., Lucarelli, F., Mann, G., McFiggans, G., Miller, M. R., Mills, G., Monk, P., Nemitz,
528 E., O'Connor, F., Ouyang, B., Palmer, P. I., Percival, C., Popoola, O., Reeves, C., Rickard, A.
529 R., Shao, L. Y., Shi, G. Y., Spracklen, D., Stevenson, D., Sun, Y. L., Sun, Z. W., Tao, S., Tong,
530 S. R., Wang, Q. Q., Wang, W. H., Wang, X. M., Wang, X. J., Wang, Z. F., Wei, L. F., Whalley,
531 L., Wu, X. F., Wu, Z. J., Xie, P. H., Yang, F. M., Zhang, Q., Zhang, Y. L., Zhang, Y. H., and
532 Zheng, M.: Introduction to the special issue “In-depth study of air pollution sources and
533 processes within Beijing and its surrounding region (APHH-Beijing)”, *Atmos. Chem. Phys.*,
534 19, 7519–7546, 2019.
- 535 Shrivastava, M., Cappa, C. D., Fan, J. W., Goldstein, A. H., Guenther, A. B., Jimenez, J. L., Kuang,
536 C., Laskin, A., Martin, S. T., Ng, N. L., Petaja, T., Pierce, J. R., Rasch, P. J., Roldin, P., Seinfeld,
537 J. H., Shilling, J., Smith, J. N., Thornton, J. A., Volkamer, R., Wang, J., Worsnop, D. R., Zaveri,
538 R. A., Zelenyuk, A., and Zhang, Q.: Recent advances in understanding secondary organic
539 aerosol: implications for global climate forcing, *Rev. Geophys.*, 55, 509–559, 2017.
- 540 Song, S. J., Gao, M., Xu, W. Q., Shao, J. Y., Shi, G. L., Wang, S. X., Wang, Y. X., Sun, Y. L., and
541 McElroy, M. B.: Fine-particle pH for Beijing winter haze as inferred from different
542 thermodynamic equilibrium models, *Atmos. Chem. Phys.*, 18, 7423–7438, 2018.
- 543 Su, H., Cheng, Y. F., and Pöschl, U.: New multiphase chemical processes influencing atmospheric
544 aerosols, air quality, and climate in the Anthropocene, *Acc. Chem. Res.*, 53, 2034–2043, 2020.
- 545 Sun, Y. L., Jiang, Q., Wang, Z. F., Fu, P. Q., Li, J., Yang, T., and Yin, Y.: Investigation of the sources
546 and evolution processes of severe haze pollution in Beijing in January 2013, *J. Geophys. Res.*
547 *Atmos.*, 119, 4380–4398, 2014.
- 548 Sun, Y. L., Wang, Z. F., Fu, P. Q., Jiang, Q., Yang, T., Li, J., and Ge, X. L.: The impact of relative
549 humidity on aerosol composition and evolution processes during wintertime in Beijing, China,
550 *Atmos. Environ.*, 77, 927–934, 2013.
- 551 Sun, Y. L., Xu, W. Q., Zhang, Q., Jiang, Q., Canonaco, F., Prévôt, A. S. H., Fu, P. Q., Li, J., Jayne,
552 J., Worsnop, D. R., and Wang, Z. F.: Source apportionment of organic aerosol from 2-year
553 highly time-resolved measurements by an aerosol chemical speciation monitor in Beijing,



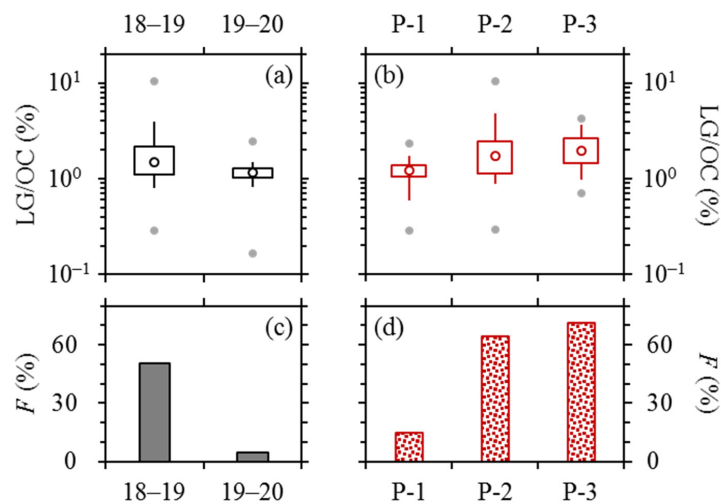
- 554 China, *Atmos. Chem. Phys.*, 18, 8469–8489, 2018.
- 555 Wang, G. H., Zhang, R. Y., Gomez, M. E., Yang, L. X., Zamora, M. L., Hu, M., Lin, Y., Peng, J. F.,
556 Guo, S., Meng, J. J., Li, J. J., Cheng, C. L., Hu, T. F., Ren, Y. Q., Wang, Y. S., Gao, J., Cao, J.
557 J., An, Z. S., Zhou, W. J., Li, G. H., Wang, J. Y., Tian, P. F., Marrero-Ortiz, W., Secret, J., Du,
558 Z. F., Zheng, J., Shang, D. J., Zeng, L. M., Shao, M., Wang, W. G., Huang, Y., Wang, Y., Zhu,
559 Y. J., Li, Y. X., Hu, J. X., Pan, B. W., Cai, L., Cheng, Y. T., Ji, Y. M., Zhang, F., Rosenfeld, D.,
560 Liss, P. S., Duce, R. A., Kolb, C. E., and Molina, M. J.: Persistent sulfate formation from
561 London Fog to Chinese haze, *Proc. Natl. Acad. Sci. U.S.A.*, 113, 13630–13635, 2016.
- 562 Wang, J. F., Li, J. Y., Ye, J. H., Zhao, J., Wu, Y. Z., Hu, J. L., Liu, D. T., Nie, D. Y., Shen, F. Z.,
563 Huang, X. P., Huang, D. D., Ji, D. S., Sun, X., Xu, W. Q., Guo, J. P., Song, S. J., Qin, Y. M.,
564 Liu, P. F., Turner, J. R., Lee, H. C., Hwang, S., Liao, H., Martin, S. T., Zhang, Q., Chen, M. D.,
565 Sun, Y. L., Ge, X. L., and Jacob, D. J.: Fast sulfate formation from oxidation of SO₂ by NO₂
566 and HONO observed in Beijing haze, *Nat. Commun.*, 11, 2844, 2020a.
- 567 Wang, J. F., Ye, J. H., Zhang, Q., Zhao, J., Wu, Y. Z., Li, J. Y., Liu, D. T., Li, W. J., Zhang, Y. G.,
568 Wu, C., Xie, C. H., Qin, Y. M., Lei, Y. L., Huang, X. P., Guo, J. P., Liu, P. F., Fu, P. Q., Li, Y.
569 J., Lee, H. C., Choi, H., Zhang, J., Liao, H., Chen, M. D., Sun, Y. L., Ge, X. L., Martin, S. T.,
570 and Jacob, D. J.: Aqueous production of secondary organic aerosol from fossil-fuel emissions
571 in winter Beijing haze, *Proc. Natl. Acad. Sci. U. S. A.*, 118, e2022179118, 2021a.
- 572 Wang, P. F., Chen, K. Y., Zhu, S. Q., Wang, P., and Zhang, H. L.: Severe air pollution events not
573 avoided by reduced anthropogenic activities during COVID-19 outbreak, *Resour. Conserv.
574 Recy.*, 158, 104814, 2020b.
- 575 Wang, W. G., Liu, M. Y., Wang, T. T., Song, Y., Zhou, L., Cao, J. J., Hu, J. N., Tang, G. G., Chen,
576 Z., Li, Z. J., Xu, Z. Y., Peng, C., Lian, C. F., Chen, Y., Pan, Y. P., Zhang, Y. H., Sun, Y. L., Li,
577 W. J., Zhu, T., Tian, H. Z., and Ge, M. F.: Sulfate formation is dominated by manganese-
578 catalyzed oxidation of SO₂ on aerosol surfaces during haze events, *Nat. Commun.*, 12, 1993,
579 2021b.
- 580 Wang, Y. J., Hu, M., Xu, N., Qin, Y. H., Wu, Z. J., Zeng, L. W., Huang, X. F., and He, L. Y.: Chemical
581 composition and light absorption of carbonaceous aerosols emitted from crop residue burning:
582 influence of combustion efficiency, *Atmos. Chem. Phys.*, 20, 13721–13734, 2020c.
- 583 Wang, Y. X., Zhang, Q. Q., Jiang, J. K., Zhou, W., Wang, B. Y., He, K. B., Duan, F. K., Zhang, Q.,



- 584 Philip, S., and Xie, Y. Y.: Enhanced sulfate formation during China's severe winter haze episode
585 in January 2013 missing from current models, *J. Geophys. Res. Atmos.*, 119, 10425–10440,
586 2014.
- 587 Xu, W. Q., Sun, Y. L., Wang, Q. Q., Zhao, J., Wang, J. F., Ge, X. L., Xie, C. H., Zhou, W., Du, W.,
588 Li, J., Fu, P. Q., Wang, Z. F., Worsnop, D. R., and Coe, H.: Changes in aerosol chemistry from
589 2014 to 2016 in winter in Beijing: insights from high-resolution aerosol mass spectrometry, *J.*
590 *Geophys. Res. Atmos.*, 124, 1132–1147, 2019.
- 591 Ye, C., Liu, P. F., Ma, Z. B., Xue, C. Y., Zhang, C. L., Zhang, Y. Y., Liu, J. F., Liu, C. T., Sun, X.,
592 and Mu, Y. J.: High H₂O₂ concentrations observed during haze periods during the winter in
593 Beijing: importance of H₂O₂ oxidation in sulfate formation, *Environ. Sci. Technol. Lett.*, 5,
594 757–763, 2018.
- 595 Zhang, Q., Zheng, Y. X., Tong, D., Shao, M., Wang, S. X., Zhang, Y. H., Xu, X. D., Wang, J. N., He,
596 H., Liu, W. Q., Ding, Y. H., Lei, Y., Li, J. H., Wang, Z. F., Zhang, X. Y., Wang, Y. S., Cheng,
597 J., Liu, Y., Shi, Q. R., Yan, L., Geng, G. N., Hong, C. P., Li, M., Liu, F., Zheng, B., Cao, J. J.,
598 Ding, A. J., Gao, J., Fu, Q. Y., Huo, J. T., Liu, B. X., Liu, Z. R., Yang, F. M., He, K. B., and
599 Hao, J. M.: Drivers of improved PM_{2.5} air quality in China from 2013 to 2017, *Proc. Natl.*
600 *Acad. Sci. U. S. A.*, 116, 24463–24469, 2019.
- 601 Zhang, R., Sun, X. S., Shi, A. J., Huang, Y. H., Yan, J., Nie, T., Yan, X., Li, X.: Secondary inorganic
602 aerosols formation during haze episodes at an urban site in Beijing, China, *Atmos. Environ.*,
603 177, 275–282, 2018.
- 604 Zheng, B., Tong, D., Li, M., Liu, F., Hong, C. P., Geng, G. N., Li, H. Y., Li, X., Peng, L. Q., Qi, J.,
605 Yan, L., Zhang, Y. X., Zhao, H. Y., Zheng, Y. X., He, K. B., and Zhang, Q.: Trends in China's
606 anthropogenic emissions since 2010 as the consequence of clean air actions, *Atmos. Chem.*
607 *Phys.*, 18, 14095–14111, 2018.
- 608 Zheng, B., Zhang, Q., Zhang, Y., He, K. B., Wang, K., Zheng, G. J., Duan, F. K., Ma, Y. L., and
609 Kimoto, T.: Heterogeneous chemistry: a mechanism missing in current models to explain
610 secondary inorganic aerosol formation during the January 2013 haze episode in North China,
611 *Atmos. Chem. Phys.*, 15, 2031–2049, 2015a.
- 612 Zheng, G. J., Duan, F. K., Su, H., Ma, Y. L., Cheng, Y., Zheng, B., Zhang, Q., Huang, T., Kimoto,
613 T., Chang, D., Pöschl, U., Cheng, Y. F., and He, K. B.: Exploring the severe winter haze in

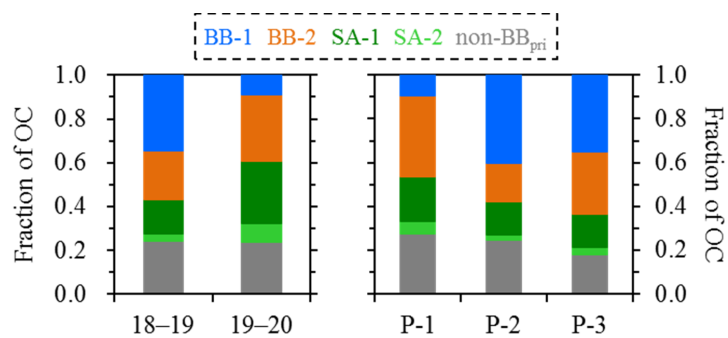


- 614 Beijing: the impact of synoptic weather, regional transport and heterogeneous reactions, *Atmos.*
615 *Chem. Phys.*, 15, 2969–2983, 2015b.
- 616 Zheng, G. J., Su, H., Wang, S. W., Andreae, M. O., Pöschl, U., and Cheng, Y. F.: Multiphase buffer
617 theory explains contrasts in atmospheric aerosol acidity, *Science*, 369, 1374–1377, 2020.



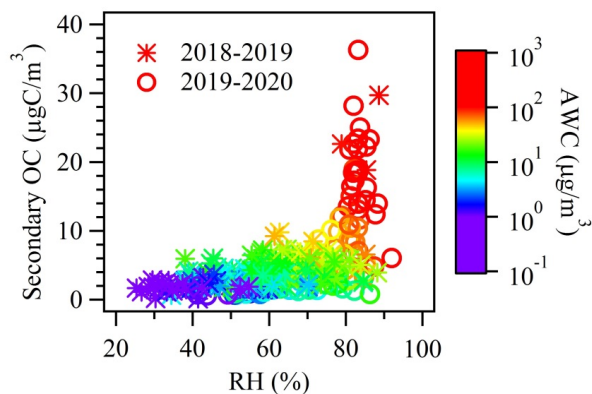
618

619 **Figure 1.** Comparisons of levoglucosan to OC ratios, i.e., LG/OC (on a basis of carbon mass), and
620 the fractions of samples with LG/OC above 1.5% (denoted as F), **(a, c)** between the 2018–2019 and
621 2019–2020 campaigns, and **(b, d)** across the 2018–2019 samples collected before (P-1), during (P-
622 2) and after (P-3) the “legitimate burning” periods. Lower and upper box bounds indicate the 25th
623 and 75th percentiles, the whiskers below and above the box indicate the 5th and 95th percentiles, the
624 solid circles below and above the box indicate the minimum and maximum, and the open circle
625 within the box marks the median (the same hereinafter).



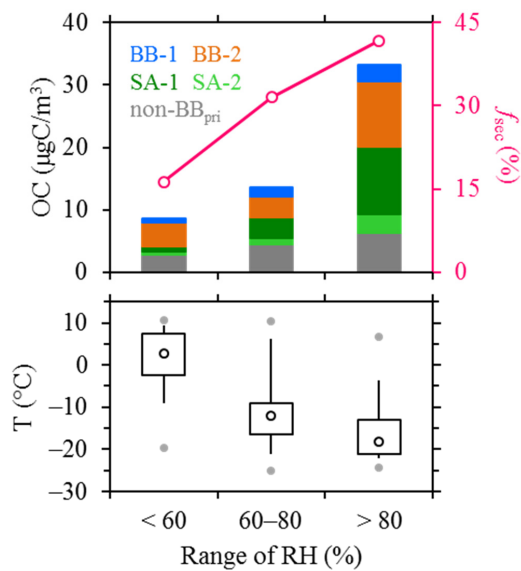
626

627 **Figure 2.** Comparison of OC source apportionment results between the 2018–2019 and 2019–2020
628 campaigns (left panel), and across the 2018–2019 samples collected before (P-1), during (P-2) and
629 after (P-3) the “legitimate burning” periods (right panel).



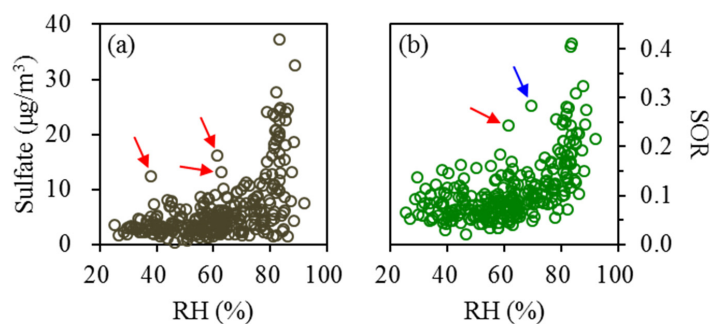
630

631 **Figure 3.** Dependence of secondary OC (OC_{sec}) on RH among the two campaigns, color-coded by
632 AWC levels. Results from the 2018–2019 campaign and 2019–2020 campaign were marked using
633 stars and circles, respectively. The majority of the data points with RH above 80% were observed
634 during 2019–2020. RH exceeded 80% for only ten samples collected during 2018–2019, and only
635 three out of these ten samples showed RH-dependent increase of OC_{sec} .



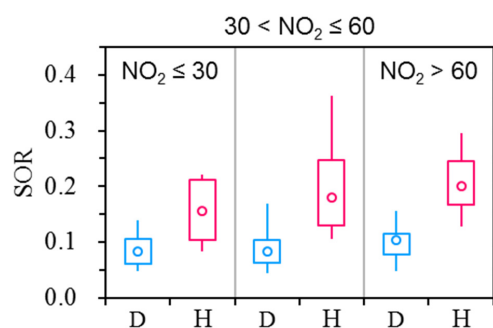
636

637 **Figure 4.** Comparisons of OC source apportionment results (upper panel, left axis), the contribution
638 of PMF-based OC_{sec} to OC (f_{sec} ; upper panel, right axis), and ambient temperatures across different
639 RH ranges (lower panel) for the 2019–2020 campaign.



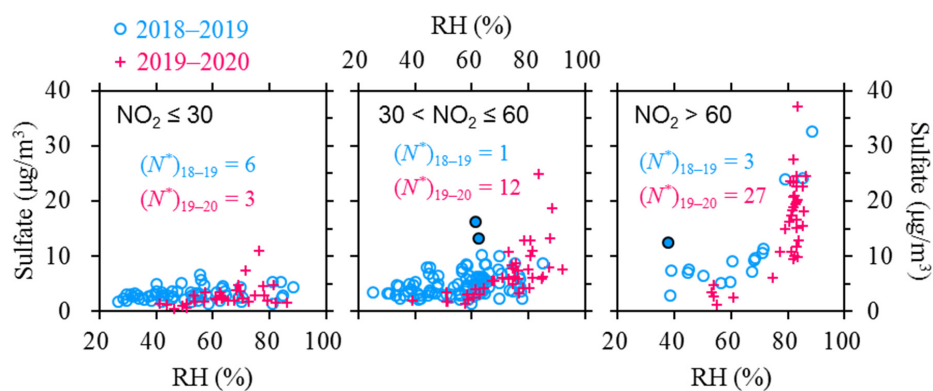
640

641 **Figure 5.** Dependences of (a) sulfate and (b) SOR on RH. Results from the 2018–2019 and 2019–
642 2020 campaigns are combined. Relatively high sulfate are typically observed for the conditions with
643 RH above 80%, which is also the case for SOR. There appear to be several outliers showing
644 considerably higher sulfate or SOR than other samples at similar RH. All the outliers occurred
645 during the 2018–2019 measurement period, and most of them were accompanied with extremely
646 high levoglucosan concentrations (above $5 \mu\text{g}/\text{m}^3$), as highlighted by the red arrows. The outlier
647 highlighted by the blue arrow was observed with ambient temperature of above $10 \text{ }^\circ\text{C}$, which was
648 uncommon for the heating season. The outliers indicate that factors other than RH were also at play
649 in sulfate formation, but the influences were evident for only several samples.

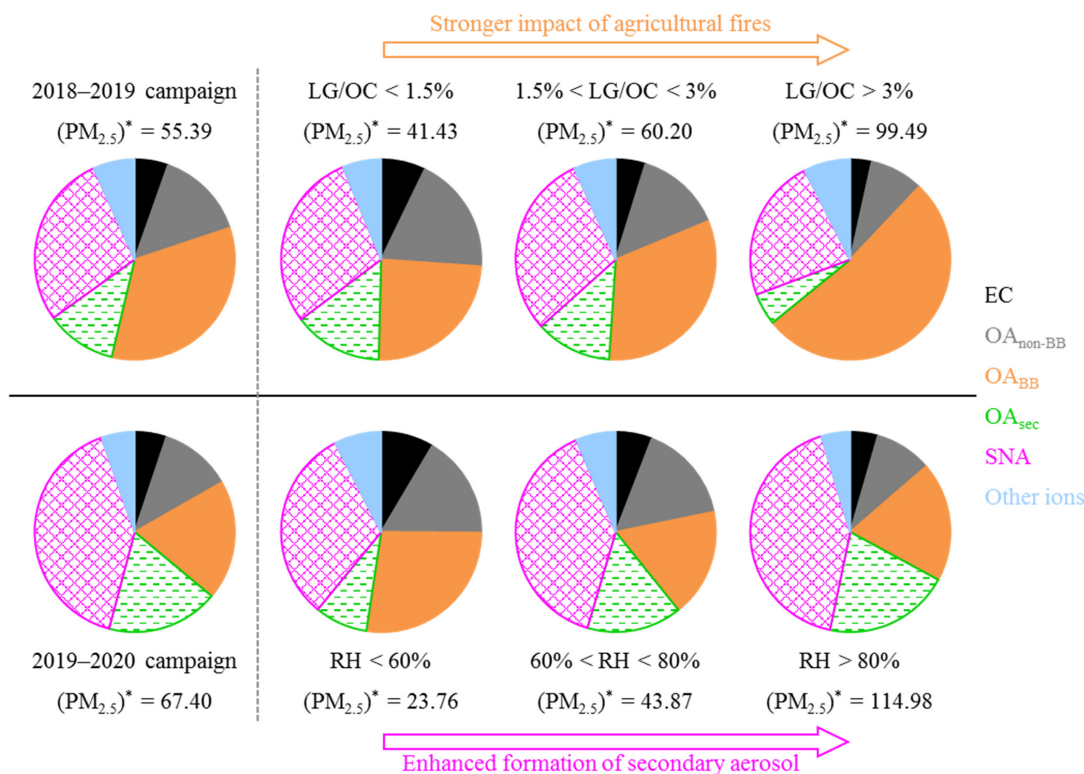


650

651 **Figure 6.** Comparisons of SOR between different RH levels, with results from different NO₂ ranges
652 (below 30, 30–60 and above 60 µg/m³) shown separately. Results from both the 2018–2019 and
653 2019–2020 campaigns are included. The terms “D” and “H” indicate relatively dry (RH below 80%)
654 and more humid conditions (RH above 80%), respectively.

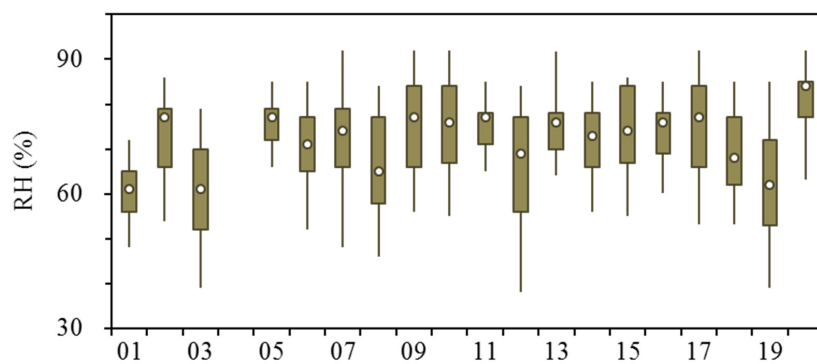


655
656 **Figure 7.** Dependences of sulfate on RH in different NO₂ ranges (below 30, 30–60 and above 60
657 µg/m³). Results from the 2018–2019 and 2019–2020 campaigns are shown using different markers.
658 The outliers in Figure 5a are highlighted by the solid circles. N* indicates the number of samples
659 with RH above 80%. High-RH conditions were typically accompanied with NO₂ concentrations of
660 below 30 µg/m³ during 2018–2019, and NO₂ above 60 µg/m³ during 2019–2020, respectively.



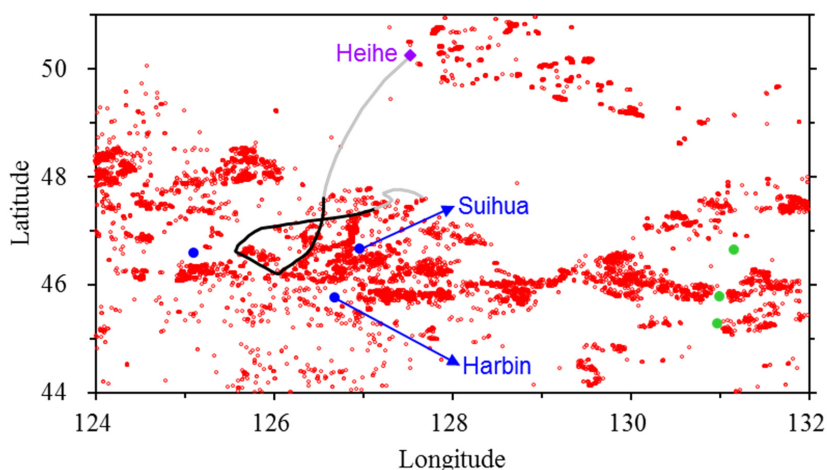
661

662 **Figure 8.** Comparison of aerosol compositions measured for the 2018–2019 and 2019–2020 campaigns. The 2018–
 663 2019 measurement period experienced relatively dry meteorological conditions (with RH levels rarely exceeding
 664 80%) and was characterized by a wide window of ~3 months for “legitimate burning”. Correspondingly, variations
 665 of $(PM_{2.5})^*$ concentration (in $\mu\text{g}/\text{m}^3$) and aerosol composition observed during 2018–2019 were mainly driven by
 666 agricultural fires. However, the “legitimate burning” policy was terminated in 2019, and the 2019–2020 campaign
 667 did not show clear evidence for apparent influence of agricultural fires. On the other hand, high-RH conditions
 668 occurred much more frequently during the 2019–2020 measurement period compared to 2018–2019.
 669 Correspondingly, variations of $(PM_{2.5})^*$ concentration and aerosol composition observed during 2019–2020 were
 670 mainly driven by RH-dependent increase of secondary aerosols.



671

672 **Figure 9.** Comparison of RH measured during January in Harbin across the past twenty years (from
673 2001 through 2020). Time resolution is 1-h for the RH data. No observational result is available for
674 January of 2004.



675

676 **Figure 10.** Active fires (red circles) detected by the joint NASA/NOAA Suomi-National Polar
677 orbiting Partnership (S-NPP) satellite for Heilongjiang Province during 17–18 April, 2020. Three
678 cities located in the Song-Nen Plain are shown using blue dots (the unlabeled city is Daqing), and
679 three cities located in the San-Jiang Plain (i.e., Shuangyashan, Qitaihe and Jixi with decreasing
680 latitudes) are shown using green dots. The two plains, separated by mountains, are the main
681 agricultural regions in Heilongjiang. Intensive agricultural fires are evident for both plains during
682 the two-day episode, indicating the open burning activities are province-wide, although prohibited.
683 The agricultural fires resulted in severe $PM_{2.5}$ pollution for nearby cities, e.g., the 24-hour
684 concentrations peaked at ~ 900 and $675 \mu\text{g}/\text{m}^3$ in Harbin and Jixi, respectively. A $PM_{2.5}$ episode
685 was observed even for Heihe (~ 500 km away from Harbin) on 19 April, 2020, which was attributed to
686 the pollutants transported from the Harbin-Suihua region. The solid line indicates the 72-hour back
687 trajectory ending at 7:00 in Heihe, accompanied with the highest 1-hour $PM_{2.5}$ observed on 19 April,
688 2020 ($\sim 310 \mu\text{g}/\text{m}^3$). The trajectory indicates transport pathway of air masses impacting Heihe,
689 with the segment in black showing locations of the air masses during 17–18 April, 2020.